

Lowering the Cu-O bond energy in CuO nanocatalysts enhances the efficiency of NH₃ oxidation

Received: 29 January 2025

Accepted: 12 September 2025

Published online: 24 October 2025

Check for updates

Lu Chen^{1,2,3}✉, Xuze Guan², Zhangyi Yao², Shusaku Hayama⁴, Matthijs A. van Spronsen⁴, Burcu Karagoz⁴, Georg Held⁴, David G. Hopkinson⁵, Christopher S. Allen^{5,6}, June Callison⁷, Paul J. Dyson⁸✉ & Feng Ryan Wang²✉

Tuning the electronic properties of nanocatalysts via doping with mono-dispersed hetero-metal atoms is an effective method used to enhance catalytic properties. Doping CuO nanoparticles with monodispersed Co atoms using different reductants affords catalysts (Co_BCu/Al₂O₃ and Co_HCu/Al₂O₃) with strikingly different electronic structures. Compared to Co_HCu/Al₂O₃, the CuO nanoparticles in Co_BCu/Al₂O₃ have longer and weaker Cu-O bonds, with a lower 1s → 4p_z antibonding transition and higher 4p → 1s bonding transition (as demonstrated from HERFD-XANES and valence-to-core X-ray emission spectroscopy). The weaker Cu-O bonds in Co_BCu/Al₂O₃ lead to superior redox activity of the CuO nanoparticles, evidenced from *operando* XAFS and in-situ near ambient pressure-near edge X-ray absorption fine structures studies. Such superior redox properties of CuO in Co_BCu/Al₂O₃ result in a much reduced activation energy of Co_BCu/Al₂O₃ compared to Co_HCu/Al₂O₃ (40.0 vs. 63.5 kJ/mol), thus leading to an enhancement in catalytic performance in the selective catalytic oxidation of NH₃ to N₂.

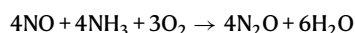
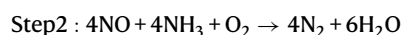
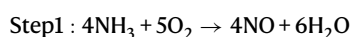
Ammonia (NH₃) emissions are projected to increase in the future, driven by its expanding use as a sustainable fuel, particularly in the shipping industry, as well as emissions from industrial processes^{1,2}. Since NH₃ emissions are far less regulated than fossil fuel-based emissions, they are an important driver for fine particulate matter (PM 2.5) pollution^{3,4}. Hence, the selective catalytic oxidation (SCO) of NH₃ to N₂ is a critical and increasingly used technology for mitigating NH₃ emissions that are detrimental to atmospheric quality⁵. This is because NH₃-assisted selective catalytic reduction (SCR) is the most widely used technology to reduce nitrogen oxide (NO_x) emissions from coal-fired power stations and diesel engines^{6–8}. Achieving

complete NO_x removal necessitates an excess of NH₃, which results in NH₃ emissions (also referred to as NH₃ slip). The completion of an NH₃-SCO cycle comprises several elementary reaction steps that depend on both the properties of the catalysts and the reaction conditions, and are crucial in controlling the selectivity to N₂. Three established mechanisms for different catalysts in the NH₃-SCO reaction include the internal SCR (i-SCR) mechanism, the imide mechanism, and the hydrazine mechanism^{9–11}. Among these, the i-SCR mechanism is predominantly applied to elucidate the NH₃-SCO reaction pathway of Cu-based catalysts^{12–16}, known for their cost-effectiveness and high selectivity.

¹Low-Carbon Conversion Science and Engineering Center, Shanghai Advanced Research Institute, Chinese Academy of Sciences, Shanghai, China.

²Department of Chemical Engineering, University College London, Roberts Building, Torrington Place, London, UK. ³Yusuf Hamied Department of Chemistry, University of Cambridge, Cambridge, UK. ⁴Diamond Light Source Ltd., Harwell Science and Innovation Campus, Chilton, Didcot, UK. ⁵electron Physical Science Imaging Centre, Diamond Light Source Ltd., Didcot, UK. ⁶Department of Materials, University of Oxford, Oxford, UK. ⁷UK Catalysis Hub, Research Complex at Harwell (RCAH), Rutherford Appleton Laboratory, Harwell, UK. ⁸Institute of Chemical Sciences and Engineering, École Polytechnique Fédérale de Lausanne (EPFL), Lausanne, Switzerland. ✉e-mail: chenlu@sari.ac.cn; paul.dyson@epfl.ch; ryan.wang@ucl.ac.uk

In the i-SCR mechanism, NH_3 undergoes initial oxidation to form NO (Step 1), and subsequently, the formed NO reacts with NH_3 , yielding N_2 (SCR, Step 2). Step 1 involves redox processes of the metal catalyst and comprises the rate-determining step in NH_3 oxidation¹⁶. Supported CuO nanoparticles (NPs) exhibit high activity and selectivity for the subsequent SCR step^{17–21}, but are less active for Step 1. In contrast, supported noble metals and Co_3O_4 NPs exhibit high activity in Step 1, but are less efficient in the SCR step (Step 2)^{22–26}. This imbalance can be overcome by integrating two metals to form a bimetallic catalyst to coordinate the sequential reactions, resulting in enhanced activity and selectivity for the entire NH_3 -SCO reaction. Several bimetallic NP catalysts have been explored for the NH_3 -SCO reaction, including those based on PtCu^{27–29}, AgCu^{30,31}, AuCu³², and RuCu.³³ Despite the high activity of noble metal-containing catalysts, their high cost and low selectivity limit practical applications. Earth-abundant CoO_x offers a cost-effective alternative, with the introduction of Cu into CoO_x improving the N_2 selectivity of CoO_x -based catalysts^{13,34}.



The activity and the selectivity of bimetallic catalysts are significantly influenced by their geometric and electronic structures^{35–37}. The different electronic structures lead to differences in the strength of the metal–oxygen bond, which determines the distribution of ammonia oxidation products^{38,39}. Oxides with high metal–oxygen bond strengths exhibit lower rates of reaction and facilitate a high selectivity to N_2 . In contrast, metal oxides with weak metal–oxygen bond strengths lead to the formation of NO_x (NO and N_2O). The unique structural features of single-site doped bimetallic NPs allow their electronic properties to be tuned more precisely than their monometallic counterparts, which provides a facile approach to modify the metal–oxygen bond strength in order to optimize both activity and N_2 selectivity⁴⁰. Note that it has previously been shown that the nature of the reducing agent impacts the catalyst structure and activity^{41,42}.

In this work, the electronic structure of two bimetallic catalysts, $\text{Co}_B\text{Cu}/\text{Al}_2\text{O}_3$ and $\text{Co}_H\text{Cu}/\text{Al}_2\text{O}_3$, prepared using NaBH_4 and H_2 , respectively, is studied with a range of X-ray spectroscopic techniques. Despite with same chemical composition, $\text{Co}_B\text{Cu}/\text{Al}_2\text{O}_3$ exhibits enhanced activity in the NH_3 -SCO reaction across all temperatures, surpassing the $\text{Co}_H\text{Cu}/\text{Al}_2\text{O}_3$ catalyst. *Operando* X-ray absorption fine structure (XAFS) studies, combined with in-situ near ambient pressure–near edge X-ray absorption fine structure (NAP-NEXAFS) studies and *operando* diffuse reflectance infrared Fourier transform spectroscopy (DRIFTS), provide a detailed understanding of the electronic structure of the CuO NPs modulated by the single Co sites and the resulting impact on catalysis.

Results and Discussion

Synthesis and structural characterization of the catalysts

The bimetallic $\text{Co}_B\text{Cu}/\text{Al}_2\text{O}_3$ catalyst (5 wt% Cu, 0.1 wt% Co) was synthesized by reducing $\text{Cu}(\text{NO}_3)_2 \cdot 3\text{H}_2\text{O}$ and $\text{Co}(\text{NO}_3)_2 \cdot 6\text{H}_2\text{O}$ together with NaBH_4 . $\text{Co}_H\text{Cu}/\text{Al}_2\text{O}_3$, with the same chemical composition, was synthesized by wet impregnation, using H_2 as a reductant. The Cu NPs are oxidized to CuO NPs when exposed to air. As shown in bright-field (BF) images and high-angle annular dark-field (HAADF) images from scanning transmission electron microscopy (STEM), the average size of the CuO NPs in $\text{Co}_B\text{Cu}/\text{Al}_2\text{O}_3$ is 2.6 nm, whereas in $\text{Co}_H\text{Cu}/\text{Al}_2\text{O}_3$ the average size is 2.0 nm (Fig. 1a–d, Supplementary Figs. S1 and S2). The size of the NPs hardly changes after catalysis for both $\text{Co}_B\text{Cu}/\text{Al}_2\text{O}_3$ (Fig. S3) and $\text{Co}_H\text{Cu}/\text{Al}_2\text{O}_3$ (Fig. S4). The interplanar spacing of the CuO lattice in $\text{Co}_B\text{Cu}/\text{Al}_2\text{O}_3$ (2.0 Å) is slightly longer than in $\text{Co}_H\text{Cu}/\text{Al}_2\text{O}_3$ (1.9 Å), indicating potentially different Cu–O bond lengths in the two catalysts (Fig. 1a–d). An energy-dispersive spectrometry (EDS) map of $\text{Co}_B\text{Cu}/\text{Al}_2\text{O}_3$ shows a uniform elemental distribution confirming the presence of Cu and Co (Fig. S5).

Electron paramagnetic resonance (EPR) spectroscopy also confirmed that the major Cu species in both catalysts comprise NPs and not monodispersed Cu sites (Fig. S6). X-ray diffraction patterns of $\text{Co}_B\text{Cu}/\text{Al}_2\text{O}_3$ and $\text{Co}_H\text{Cu}/\text{Al}_2\text{O}_3$ show no obvious distinctions from the Al_2O_3 support (PDF #10-0425) (Fig. S7a), indicative of small NPs with a uniform size distribution. H_2 -temperature programmed reduction (TPR) confirms that incorporation of Co atoms in $\text{Co}_B\text{Cu}/\text{Al}_2\text{O}_3$ shifts the reduction temperature of CuO NPs by 34 °C (first peak) to a lower temperature (Fig. S8), indicating that Co promotes the reduction of

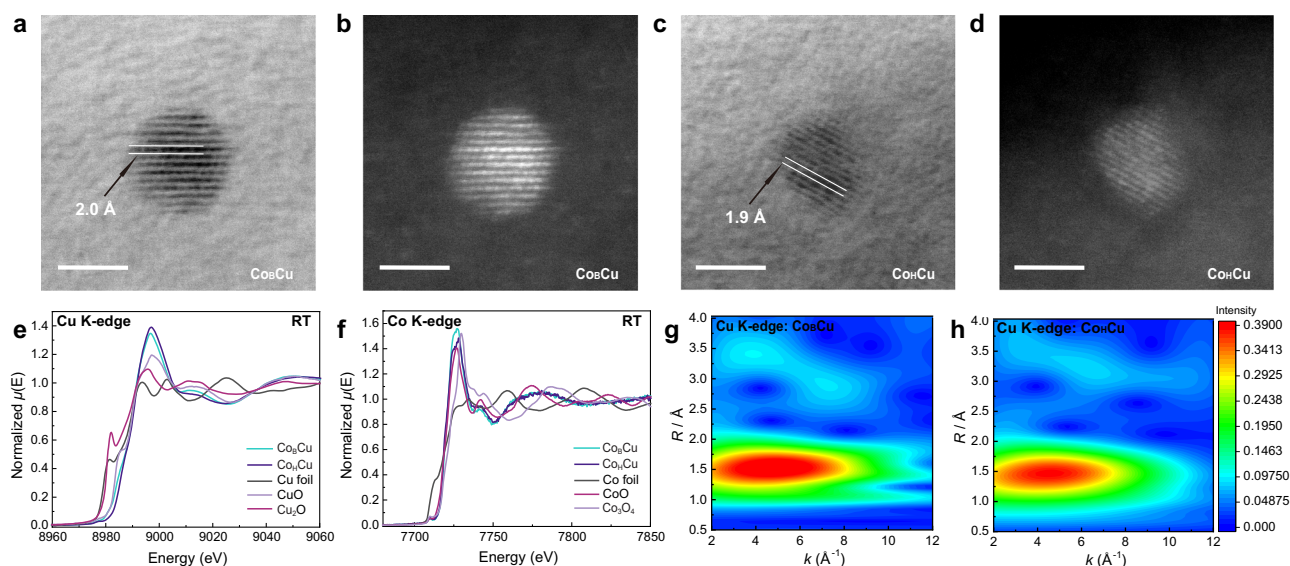


Fig. 1 | Characterization of $\text{Co}_B\text{Cu}/\text{Al}_2\text{O}_3$ and $\text{Co}_H\text{Cu}/\text{Al}_2\text{O}_3$. BF images (a) and HAADF image (b) of $\text{Co}_B\text{Cu}/\text{Al}_2\text{O}_3$ (Scale bar = 2 nm); BF image (c) and HAADF image (d) of $\text{Co}_H\text{Cu}/\text{Al}_2\text{O}_3$ (Scale bar = 2 nm); Cu K-edge HERFD-XANES (e) and Co

K-edge XANES (f) of $\text{Co}_B\text{Cu}/\text{Al}_2\text{O}_3$ and $\text{Co}_H\text{Cu}/\text{Al}_2\text{O}_3$; 2D WT-EXAFS maps of the CuO NPs in $\text{Co}_B\text{Cu}/\text{Al}_2\text{O}_3$ (g) and $\text{Co}_H\text{Cu}/\text{Al}_2\text{O}_3$ (h).

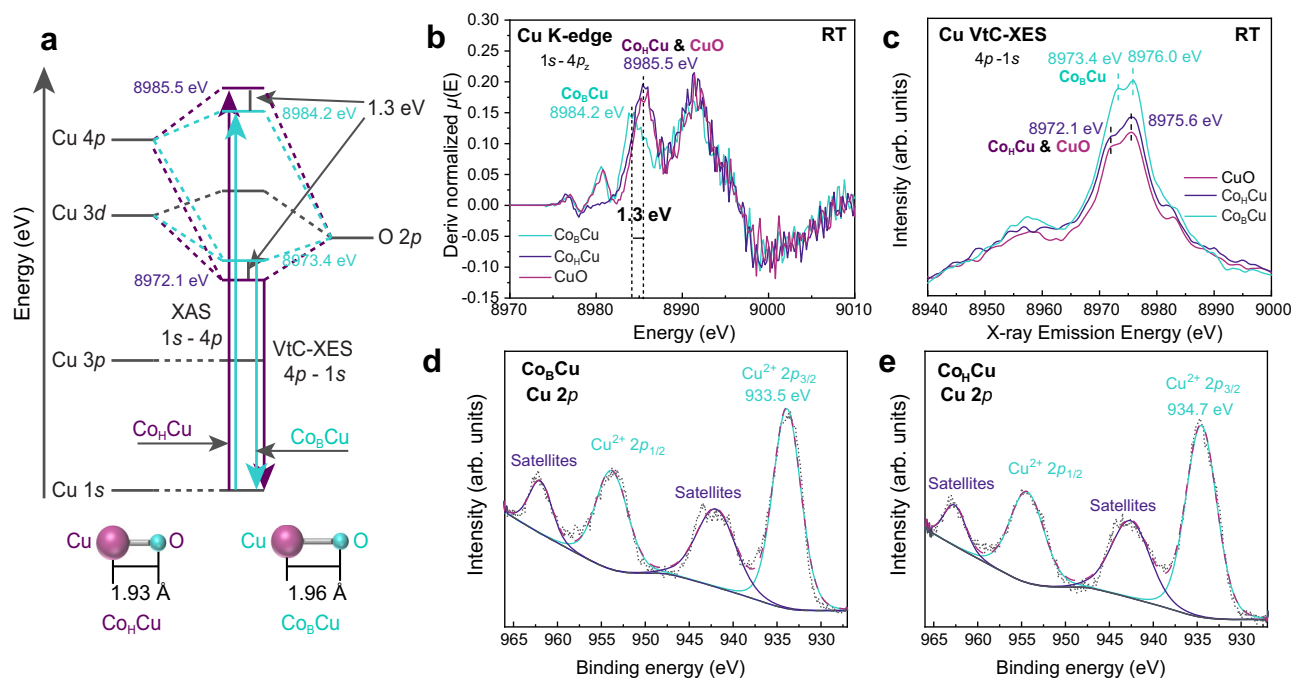


Fig. 2 | Characterization of $\text{Co}_B\text{Cu}/\text{Al}_2\text{O}_3$ and $\text{Co}_H\text{Cu}/\text{Al}_2\text{O}_3$. **a** simplified molecular orbital diagram of the CuO NPs in $\text{Co}_B\text{Cu}/\text{Al}_2\text{O}_3$ and $\text{Co}_H\text{Cu}/\text{Al}_2\text{O}_3$; **b** first derivative XANES spectra and **c** VtC-XES of $\text{Co}_B\text{Cu}/\text{Al}_2\text{O}_3$, $\text{Co}_H\text{Cu}/\text{Al}_2\text{O}_3$, and $\text{CuO}/\text{Al}_2\text{O}_3$; **d** $\text{Cu } 2p$ XPS spectra of $\text{Co}_B\text{Cu}/\text{Al}_2\text{O}_3$ (**d**) and $\text{Co}_H\text{Cu}/\text{Al}_2\text{O}_3$ (**e**).

CuO , probably via the asymmetric Co-O-Cu bond⁴³. In contrast, for $\text{Co}_H\text{Cu}/\text{Al}_2\text{O}_3$, two separate peaks indicate weaker interactions between the Cu and Co species. The broad peak in the T range of 200–300 °C of $\text{Co}_B\text{Cu}/\text{Al}_2\text{O}_3$ in H_2 -TPR may originate from bulk CoO_x , due to the aggregation of Co under H_2 .

The chemical environments of the Cu species in $\text{Co}_B\text{Cu}/\text{Al}_2\text{O}_3$ and $\text{Co}_H\text{Cu}/\text{Al}_2\text{O}_3$ are different, as determined from extended X-ray absorption fine structure (EXAFS), X-ray absorption near-edge structure (XANES), and high-energy resolution fluorescence detected - X-ray absorption near-edge structure (HERFD-XANES) measurements (Fig. 1e, f). The major Cu species in both $\text{Co}_B\text{Cu}/\text{Al}_2\text{O}_3$ and $\text{Co}_H\text{Cu}/\text{Al}_2\text{O}_3$ are Cu^{2+} , as expected for CuO-based NPs, and the Co species in both $\text{Co}_B\text{Cu}/\text{Al}_2\text{O}_3$ and $\text{Co}_H\text{Cu}/\text{Al}_2\text{O}_3$ are also in the Co^{2+} oxidation state. The fitted EXAFS data reveal differences between the electronic structures of $\text{Co}_B\text{Cu}/\text{Al}_2\text{O}_3$ and $\text{Co}_H\text{Cu}/\text{Al}_2\text{O}_3$ (Table S1, Figs. S9–S11). $\text{Co}_B\text{Cu}/\text{Al}_2\text{O}_3$ and $\text{Co}_H\text{Cu}/\text{Al}_2\text{O}_3$ have a similar Cu-O coordination number (C.N.) of 3.45 ± 0.12 and 3.33 ± 0.12 , respectively, and a similar Co-O C.N. of 5.74 ± 0.99 and 5.92 ± 1.09 , respectively. However, $\text{Co}_B\text{Cu}/\text{Al}_2\text{O}_3$ has a larger Cu-Cu (1) C.N. of 2.39 ± 0.48 and a Cu-Cu (2) C.N. of 1.90 ± 0.39 , compared to $\text{Co}_H\text{Cu}/\text{Al}_2\text{O}_3$ with a Cu-Cu (1) C.N. of 0.22 ± 0.21 and Cu-Cu (2) C.N. of 0. Moreover, the Cu-O bond length in $\text{Co}_B\text{Cu}/\text{Al}_2\text{O}_3$ ($1.96 \text{ \AA} \pm 0.005$) is longer than in $\text{Co}_H\text{Cu}/\text{Al}_2\text{O}_3$ ($1.93 \text{ \AA} \pm 0.003$), which is consistent with the TEM results. It is noteworthy that Co-Co bonds are not observed in either catalyst, indicative of single Co sites. Wavelet transform (WT) analysis of the EXAFS spectra leads to a 2D representation of the EXAFS (Fig. 1g, h), simultaneously revealing the signal features in both R- and k-space. The first shell peak with the most intense signal in $\text{Co}_B\text{Cu}/\text{Al}_2\text{O}_3$ (centered at 4.7 \AA^{-1} , 1.52 \AA) is higher than the equivalent peak in $\text{Co}_H\text{Cu}/\text{Al}_2\text{O}_3$ (centered at 4.5 \AA^{-1} , 1.46 \AA). This difference further confirms that $\text{Co}_B\text{Cu}/\text{Al}_2\text{O}_3$ has longer Cu-O bonds, as the first shell is assigned to oxygen atoms coordinated to the copper.

The electronic structures of $\text{Co}_B\text{Cu}/\text{Al}_2\text{O}_3$ and $\text{Co}_H\text{Cu}/\text{Al}_2\text{O}_3$ were established using HERFD-XANES, valence-to-core X-ray emission spectroscopy (VtC-XES) and fine-scanned X-ray photoelectron spectroscopy (XPS) measurements (Figs. 2, S7). First derivative XANES contains a $1s \rightarrow 4p_z$ transition at 8984.2 eV for $\text{Co}_B\text{Cu}/\text{Al}_2\text{O}_3$ (Fig. 2b),

which is 1.3 eV lower than in $\text{Co}_H\text{Cu}/\text{Al}_2\text{O}_3$ and $\text{CuO}/\text{Al}_2\text{O}_3$. In previous studies^{16,44}, the absorption energy for the $1s \rightarrow 4p_z$ transition was shown to increase as the CuO loading decreases (from NPs to atomic sites), whereas a decrease in the $1s \rightarrow 4p_z$ transition energy is rarely observed. This discrepancy suggests a different local coordination environment of Cu^{2+} in $\text{Co}_B\text{Cu}/\text{Al}_2\text{O}_3$ (Fig. 2b). Furthermore, VtC-XES reveals that the CuO NPs in $\text{Co}_B\text{Cu}/\text{Al}_2\text{O}_3$ have a 1.3 eV higher Cu $K_{\beta 2,5}$ feature (mainly $4p \rightarrow 1s$ transitions) than the CuO NPs in $\text{Co}_H\text{Cu}/\text{Al}_2\text{O}_3$ and $\text{CuO}/\text{Al}_2\text{O}_3$ (Fig. 2c). The distribution of Cu $4p$ states is markedly influenced by the hybridization between Cu $3d$ and ligand p states⁴⁵. For Cu^{2+} species, the low-energy peak observed in the main $K_{\beta 2,5}$ line primarily arises from the contribution of the π -bonding state⁴⁵, which results from the hybridization of Cu $3d$, O $2p$ and Cu $4p$ orbitals. The lower $1s \rightarrow 4p_z$ transition energy and higher π -bonding state of $\text{Co}_B\text{Cu}/\text{Al}_2\text{O}_3$ point to different occupied and unoccupied states (Fig. 2a). Additionally, XPS of $\text{Co}_B\text{Cu}/\text{Al}_2\text{O}_3$, $\text{Co}_H\text{Cu}/\text{Al}_2\text{O}_3$, $\text{CuO}/\text{Al}_2\text{O}_3$, and $\text{CoCu}/\text{Al}_2\text{O}_3$ exhibit $\text{Cu}^{2+} 2p_{3/2}$ peaks at 933.5, 934.7, 934.6, and 934.7 eV, respectively (Figs. 2d, e, S7c, d). Thus, the electronic states of Cu in Cu_HCo , $\text{CuO}/\text{Al}_2\text{O}_3$, and $\text{CoCu}/\text{Al}_2\text{O}_3$ are similar, with that of Cu_BCo being lower (Fig. S7c). The combination of HERFD-XANES, VtC-XES, and XPS suggests that the Cu-O bonds in the $\text{Co}_B\text{Cu}/\text{Al}_2\text{O}_3$ catalyst are weakened relative to those observed in $\text{Co}_H\text{Cu}/\text{Al}_2\text{O}_3$ (Fig. 2a), which is as expected, as the Cu-O bonds in $\text{Co}_B\text{Cu}/\text{Al}_2\text{O}_3$ are longer (Fig. 1g, h). This feature indicates that the Cu-O bonds in $\text{Co}_B\text{Cu}/\text{Al}_2\text{O}_3$ will be more reactive toward NH_3 , leading to the reduction of Cu^{2+} and concomitant oxidation of NH_3 . As proven in our recent publication, such a reaction is the rate-limiting step in the i-SCR mechanism⁴⁶. Literature further supports this by showing that metal oxides with high metal-oxygen bond strengths exhibit lower rates in the NH_3 -SCO reaction⁴⁷.

Evaluation of the catalysts in the NH_3 -SCO reaction

The catalytic performance of the bimetallic $\text{Co}_B\text{Cu}/\text{Al}_2\text{O}_3$ and $\text{Co}_H\text{Cu}/\text{Al}_2\text{O}_3$ catalysts was compared with single metal $\text{CuO}/\text{Al}_2\text{O}_3$ and $\text{CoO}_x/\text{Al}_2\text{O}_3$ catalysts in the NH_3 -SCO reaction (Figs. 3a, S12 and S13). 5000 ppm NH_3 and GHSV 100,000 h^{-1} are used as the standard test conditions, which are consistent with waste gas streams in industrial processes and have been used in previous studies^{48–51}.

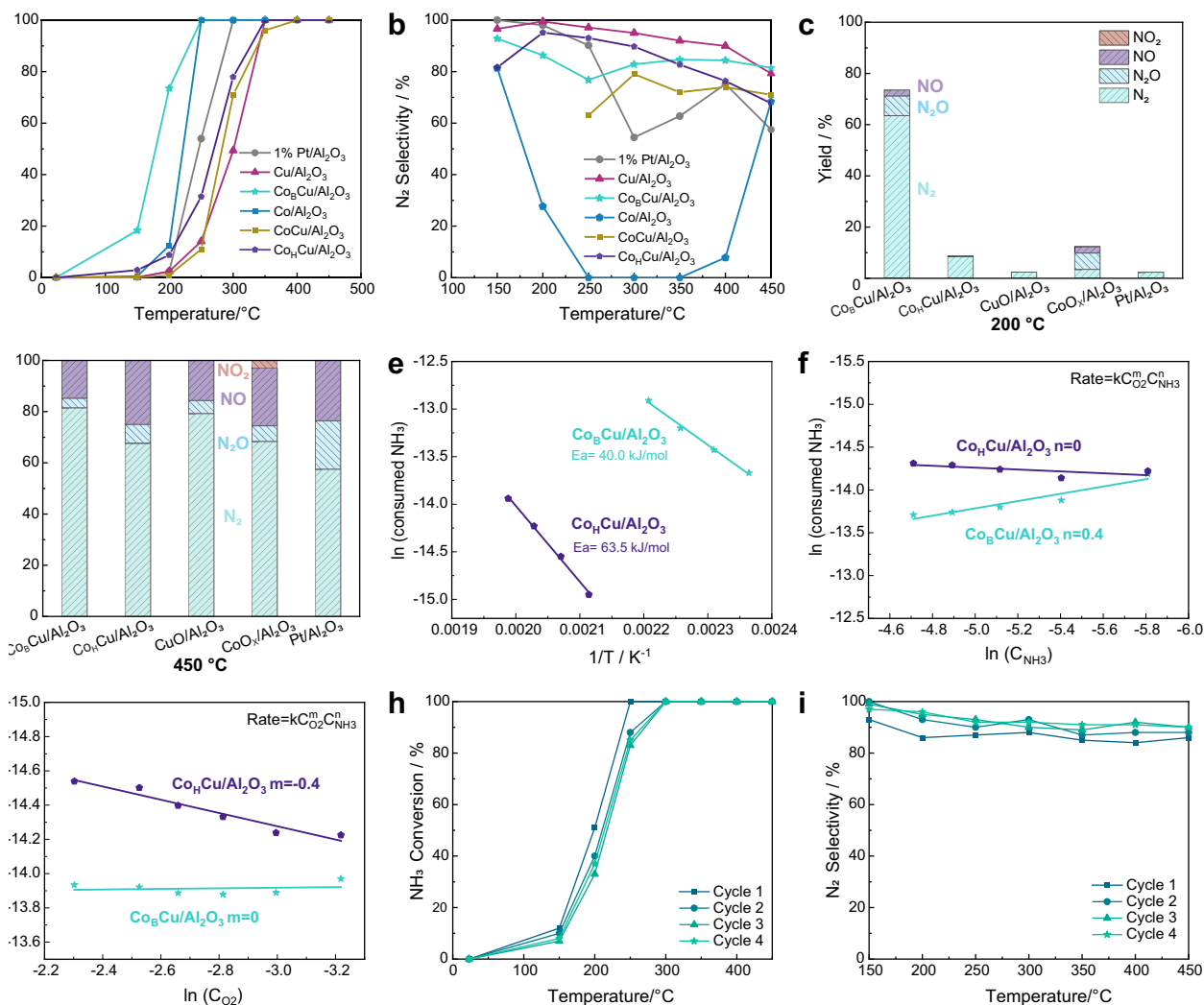


Fig. 3 | Evaluation of Co_BCu/Al₂O₃, Co_HCu/Al₂O₃ and control catalysts in the NH₃-SCO reaction. NH₃ conversion (a) and selectivity to N₂ (b) as a function of temperature (note that CoCu/Al₂O₃ corresponds to the catalyst without reduction); Product distribution at 200 °C (c) and 450 °C (d); e Activation energy for the

Co_BCu/Al₂O₃ and Co_HCu/Al₂O₃ catalyzed reaction; Reaction order for NH₃ (f) and O₂ (g); Stability tests of Co_BCu/Al₂O₃ over 4 cycles (h, i) (50 mg Co_BCu/Al₂O₃ mixed with 100 SiC). Reaction conditions: 50 mg catalyst, 5000 ppm NH₃, 5% O₂ balanced in He, gas flow: 100 mL/min, WHSV = 600 mL NH₃·h⁻¹·g⁻¹.

Among these catalysts, Co_BCu/Al₂O₃ exhibits the highest activity with the lowest T₅₀ value (i.e., the temperature that achieves 50% NH₃ conversion) of around 175 °C, with complete NH₃ conversion achieved at around 250 °C. The activities of Co_BCu/Al₂O₃ and Co_HCu/Al₂O₃ are higher than that of CoCu/Al₂O₃ (i.e., without reduction) (Fig. 3). Hence, both the addition of Co into CuO and the nature of the reductant affect the catalytic activity. Both Co_BCu/Al₂O₃ and Co_HCu/Al₂O₃ have higher activities than CuO/Al₂O₃, indicating that Co contributes to the activity (Fig. 3). Although CoO_x/Al₂O₃ (5 wt% Co loading) is more active than Co_HCu/Al₂O₃, the selectivity to N₂ is much lower, with the main products comprising NO and N₂O between 250–350 °C (Fig. S10). At 200 °C, Co_BCu/Al₂O₃ showed at least a four-fold higher activity than the other catalysts (Fig. 3c). The Co loading was evaluated in the range of 0.1 to 5% for Co_BCu/Al₂O₃. As the Co loading increases, the Co species no longer remain as single sites, and the activity of Co_{1%}Cu/Al₂O₃ (Co loading of 1 wt%) and Co_{5%}Cu/Al₂O₃ (Co loading of 5 wt%) are not as high as Co_BCu/Al₂O₃ with a Co loading of 0.1 wt% (Fig. S14). Additionally, the selectivity to N₂ for Co_BCu/Al₂O₃ was > 80%, even at high temperatures, and is lower than Co_HCu/Al₂O₃ below 350 °C, but is superior to Co_HCu/Al₂O₃ above 350 °C (Fig. 3b, d). Remarkably, despite having the same chemical composition, Co_BCu/Al₂O₃ displayed consistently higher activity than Co_HCu/Al₂O₃ across all temperature

ranges. At 200 °C, Co_BCu/Al₂O₃ achieved nearly 10 times higher NH₃ conversion than Co_HCu/Al₂O₃ (Fig. 3a). The different electronic structures lead to differences in the strength of the metal–oxygen bonds, which influence both activity and selectivity in the NH₃-SCO reaction^{38,39}. Catalysts with weaker metal–oxygen bonds tend to exhibit higher rates of reaction, but result in the formation of NO_x (NO and N₂O). Compared to Co_HCu/Al₂O₃, Co_BCu/Al₂O₃ has a lower 1s → 4p_z antibonding transition and a higher 4p → 1s bonding transition of Cu–O bonds, indicative of weaker Cu–O bonds^{52–54}. Thus, the superior activity and lower selectivity to N₂ observed for Co_BCu/Al₂O₃ may be attributed to the electronic structure of Cu²⁺ produced by the local coordination environment.

The apparent activation energy of Co_BCu/Al₂O₃ is 40.0 kJ/mol, which is lower than that of Co_HCu/Al₂O₃ with a value of 63.5 kJ/mol (Fig. 3e). This difference suggests that the superior activity of Co_BCu/Al₂O₃ in the NH₃-SCO reaction may be attributed to a reduced energy barrier for the reaction. The reaction order for NH₃ in the SCO process is 0.4 for Co_BCu/Al₂O₃, indicating partial dependence on NH₃ concentration, while it is 0 for Co_HCu/Al₂O₃ (Fig. 3f), implying that NH₃ does not influence the reaction rate under these conditions due to a much higher Cu–O bond energy. The reaction order for O₂ also differs between the catalysts, with Co_BCu/Al₂O₃ exhibiting an O₂ order of 0

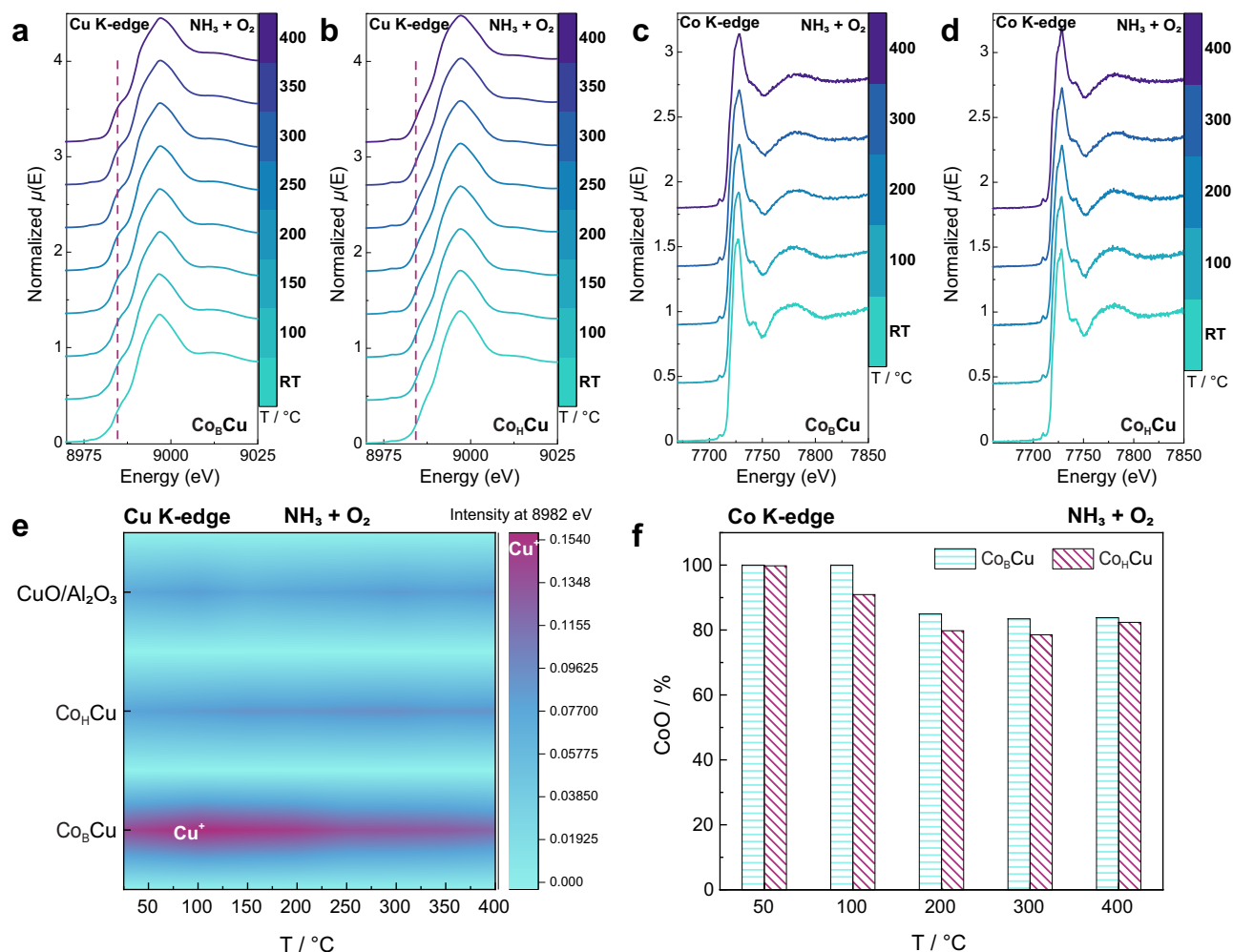


Fig. 4 | Operando studies of the redox behavior of Cu and Co in $\text{Co}_B\text{Cu}/\text{Al}_2\text{O}_3$ and $\text{Co}_H\text{Cu}/\text{Al}_2\text{O}_3$. Operando Cu K-edge XAFS of $\text{Co}_B\text{Cu}/\text{Al}_2\text{O}_3$ (a) and $\text{Co}_H\text{Cu}/\text{Al}_2\text{O}_3$ (b) as a function of temperature; operando Co K-edge XAFS of $\text{Co}_B\text{Cu}/\text{Al}_2\text{O}_3$ (c) and

$\text{Co}_H\text{Cu}/\text{Al}_2\text{O}_3$ (d); e operando Cu K-edge XAFS, signal intensity of the Cu^+ $1s \rightarrow 4p$ transition peak at 8982 eV in a NH_3/O_2 atmosphere as a function of temperature; f proportion of CoO in $\text{Co}_B\text{Cu}/\text{Al}_2\text{O}_3$ and $\text{Co}_H\text{Cu}/\text{Al}_2\text{O}_3$ as a function of temperature.

(Fig. 3g), which suggests the participation of lattice oxygen in the reaction. In contrast, $\text{Co}_H\text{Cu}/\text{Al}_2\text{O}_3$ shows an O_2 order of -0.4 (Fig. 3g), likely due to competitive adsorption between NH_3 and O_2 at active sites, which inhibits O_2 involvement in the reaction. Furthermore, $\text{Co}_B\text{Cu}/\text{Al}_2\text{O}_3$ demonstrates good stability under the reaction conditions, showing no significant decrease in catalytic activity or N_2 selectivity even after four consecutive reaction cycles. The reduced activity might be caused by the weak metal-support interactions between nanoparticles and support.

Redox properties of the CuO NPs

The redox properties of the catalyst play a crucial role in the oxidation of NH_3 , directly impacting on the overall NH_3 -SCO reaction activity⁴⁶. The performance of Cu-based catalysts is related to the $\text{Cu}^+/\text{Cu}^{2+}$ redox couple, and the activity may be correlated with the presence of Cu^+ , as observed in several Cu-based catalysts^{55,56}. Mechanistically, the reaction could be considered to proceed through the reaction of NH_3 with Cu^{2+} to form $\text{Cu}^+(\text{NH}_3)_2$ as the rate-determining step, followed by the oxidation of $\text{Cu}^+(\text{NH}_3)_2$ to Cu^{2+} .

To evaluate the redox behavior of the single Co and bulk Cu sites, and monitor structural changes under real NH_3 -SCO reaction conditions, operando XAFS was undertaken in fluorescence mode at the Co K-edge and transmission mode at the Cu K-edge under steady-state conditions at each temperature (Figs. 4, S15 and S16). The formation of reduced Cu^+ is considered to be a trigger for the NH_3 -SCO reaction. In

the Cu K-edge XAFS spectra, the evolution of the Cu^+ $1s \rightarrow 4p$ transition peak of $\text{Co}_B\text{Cu}/\text{Al}_2\text{O}_3$, $\text{Co}_H\text{Cu}/\text{Al}_2\text{O}_3$ and $\text{CuO}/\text{Al}_2\text{O}_3$ was monitored as a function of temperature during the NH_3 -SCO reaction (NH_3 5000 ppm, O_2 5%) (Fig. 4e). The Cu^{2+} in $\text{Co}_B\text{Cu}/\text{Al}_2\text{O}_3$ is partially reduced to Cu^+ , even under excess O_2 , as evidenced by the more pronounced peak intensity at Cu K-edge 8982 eV (the typical feature for $\text{Cu}^+(\text{NH}_3)_2$ $1s \rightarrow 4p$, XANES) (Fig. 4e). In contrast, the peak intensity at Cu K-edge 8982 eV in $\text{Co}_H\text{Cu}/\text{Al}_2\text{O}_3$ slightly increases, and Cu^+ is not detected throughout the entire temperature range in $\text{CuO}/\text{Al}_2\text{O}_3$ (Fig. 4e, S19 and 20). The redox activity of the single Co sites in $\text{Co}_B\text{Cu}/\text{Al}_2\text{O}_3$ and $\text{Co}_H\text{Cu}/\text{Al}_2\text{O}_3$ is similar (Fig. 4f). The single Co sites comprise Co^{2+} at room temperature and are partially oxidized to Co_3O_4 as the temperature increases. Moreover, in different gases from the most reductive, i.e., NH_3 without O_2 , to the most oxidative, i.e., $\text{NH}_3 + \text{O}_2$, the Cu species in $\text{Co}_B\text{Cu}/\text{Al}_2\text{O}_3$ are in a more reduced state than $\text{Co}_H\text{Cu}/\text{Al}_2\text{O}_3$ (Figs. S17–19), confirming the superior redox ability of the CuO NPs in $\text{Co}_B\text{Cu}/\text{Al}_2\text{O}_3$.

As the catalytically active sites are predominantly on the surface, in-situ near ambient pressure near-edge X-ray absorption fine structure (NAP-NEXAFS) was used to investigate the redox properties of the surface Cu species in $\text{Co}_B\text{Cu}/\text{Al}_2\text{O}_3$ and $\text{Co}_H\text{Cu}/\text{Al}_2\text{O}_3$ (Fig. 5). The redox activity of the Cu species in $\text{Co}_B\text{Cu}/\text{Al}_2\text{O}_3$ and $\text{Co}_H\text{Cu}/\text{Al}_2\text{O}_3$ was evaluated under $\text{NH}_3 + \text{O}_2$ at different temperatures (Fig. 5a, d). At all temperatures, $\text{Co}_B\text{Cu}/\text{Al}_2\text{O}_3$ has a more pronounced peak compared to $\text{Co}_H\text{Cu}/\text{Al}_2\text{O}_3$ at 934.2 eV corresponding to Cu^+/Cu^0 , and a broad peak

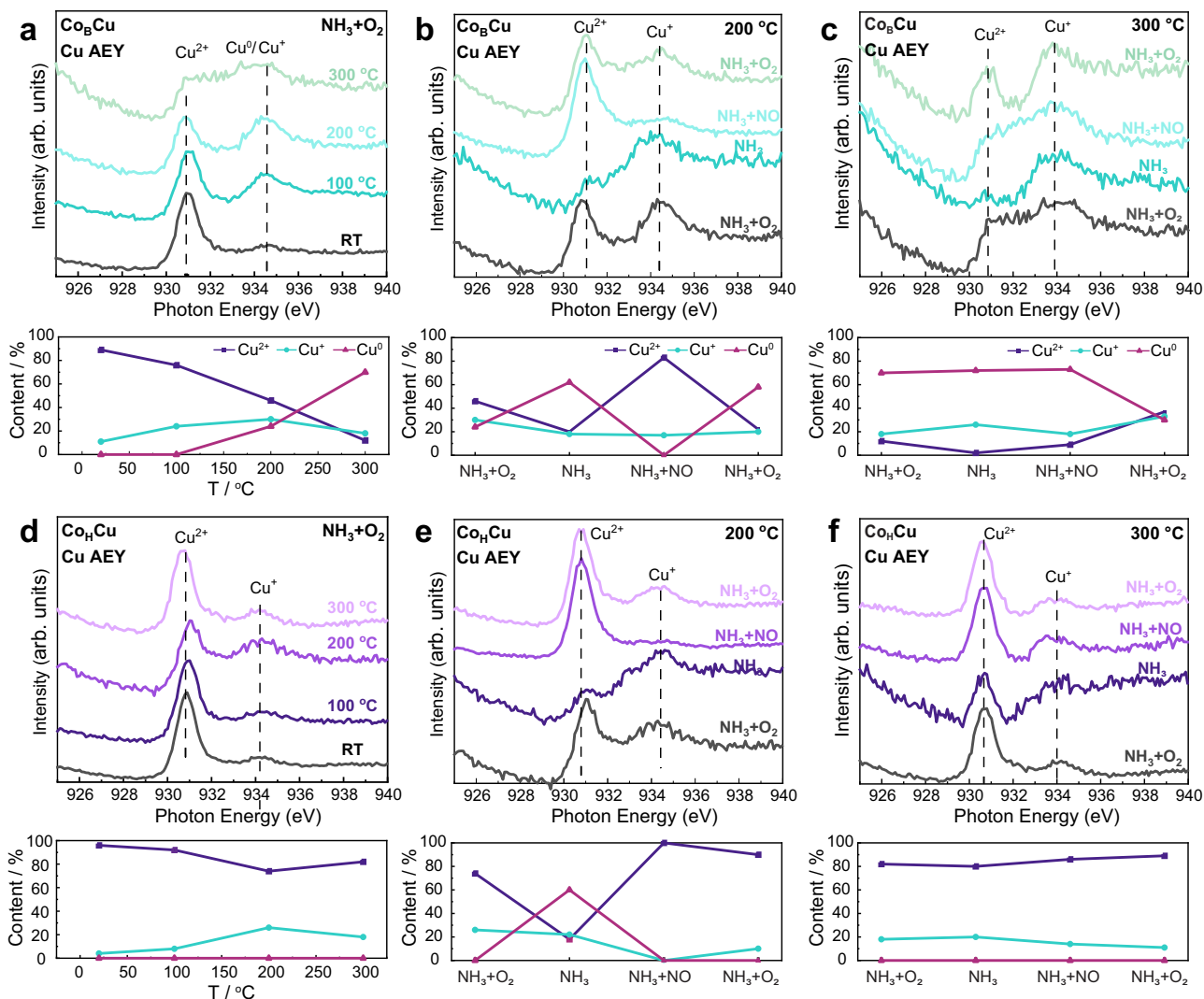


Fig. 5 | In-situ NAP-NEXAFS spectra and corresponding Cu species distribution of $\text{Co}_B\text{Cu}/\text{Al}_2\text{O}_3$ and $\text{Co}_H\text{Cu}/\text{Al}_2\text{O}_3$. **a** Cu L-edge (in Auger electron yield (AEY) mode) and corresponding Cu species content of $\text{Co}_B\text{Cu}/\text{Al}_2\text{O}_3$ under $\text{NH}_3 + \text{O}_2$ as a function of temperature; Cu L-edge and corresponding Cu species content of $\text{Co}_B\text{Cu}/\text{Al}_2\text{O}_3$ under various gas atmospheres at 200 °C (**b**) and at 300 °C (**c**) (gas

pressure 0.3 mbar); **d** Cu L-edge (AEY mode) and corresponding Cu species content of $\text{Co}_H\text{Cu}/\text{Al}_2\text{O}_3$ under $\text{NH}_3 + \text{O}_2$ as a function of temperature; Cu L-edge (AEY mode) and corresponding Cu species content of $\text{Co}_H\text{Cu}/\text{Al}_2\text{O}_3$ under various gas atmospheres at 200 °C (**e**) and at 300 °C (**f**) (gas pressure 0.3 mbar).

at 930.9 eV corresponding to Cu^{2+} . Linear combination fitting (LCF) (see standards in Fig. S20) further confirms that the proportion of reductive Cu species (Cu^+/Cu^0) in $\text{Co}_B\text{Cu}/\text{Al}_2\text{O}_3$ is higher than in $\text{Co}_H\text{Cu}/\text{Al}_2\text{O}_3$ at all temperatures. Above 200 °C, the reduced Cu species dominate in $\text{Co}_B\text{Cu}/\text{Al}_2\text{O}_3$ catalyst.

Additionally, NAP-NEXAFS of the $\text{Co}_B\text{Cu}/\text{Al}_2\text{O}_3$ and $\text{Co}_H\text{Cu}/\text{Al}_2\text{O}_3$ catalysts under different gas atmospheres further confirmed the superior redox properties of the single Cu sites in $\text{Co}_B\text{Cu}/\text{Al}_2\text{O}_3$ (Fig. 5). At 200 °C in NH_3 , the surface Cu species of both $\text{Co}_B\text{Cu}/\text{Al}_2\text{O}_3$ and $\text{Co}_H\text{Cu}/\text{Al}_2\text{O}_3$ are nearly completely reduced to Cu^+/Cu^0 . At 300 °C in NH_3 , the surface Cu species of $\text{Co}_B\text{Cu}/\text{Al}_2\text{O}_3$ are nearly completely reduced to Cu^+/Cu^0 , whereas the surface Cu species of $\text{Co}_H\text{Cu}/\text{Al}_2\text{O}_3$ are mainly in the form of Cu^{2+} . Under $\text{NH}_3 + \text{NO}$, the surface Cu species in $\text{Co}_H\text{Cu}/\text{Al}_2\text{O}_3$ are more oxidized than the surface Cu species in $\text{Co}_B\text{Cu}/\text{Al}_2\text{O}_3$, which become more reduced. Based on the *operando* XAFS and in-situ NAP-NEXAFS studies, the Cu species in the CuO NPs with weaker Cu-O bonds, as in $\text{Co}_B\text{Cu}/\text{Al}_2\text{O}_3$, exhibit superior redox properties. The longer (and hence weaker) Cu-O bonds in $\text{Co}_B\text{Cu}/\text{Al}_2\text{O}_3$ result in enhanced redox ability and, consequently, higher activity.

In-Situ DRIFTS confirms different adsorption behavior in $\text{Co}_B\text{Cu}/\text{Al}_2\text{O}_3$ and $\text{Co}_H\text{Cu}/\text{Al}_2\text{O}_3$ (Fig. 6)⁵⁷. The bands observed at 1625 and 1256 cm^{-1} may be assigned to asymmetric and symmetric deformation of ammonia chemisorbed on Lewis acid sites of Al_2O_3 , respectively²³. The peak at 1405 cm^{-1} may be assigned to NH_3 coordinated to Cu^{58,59}. The peak at 1460 cm^{-1} originates from Brønsted acid sites on Al_2O_3 . A peak at 1580 cm^{-1} gradually emerges at temperatures above 250 °C in $\text{Co}_B\text{Cu}/\text{Al}_2\text{O}_3$, which may be tentatively assigned to nitrate species, with this peak only emerging at temperatures above 300 °C in the presence of $\text{Co}_B\text{Cu}/\text{Al}_2\text{O}_3$. The unique electronic structure of the CuO NPs in $\text{Co}_B\text{Cu}/\text{Al}_2\text{O}_3$ which leads to weaker Cu-O bonds, might be an important factor for the enhanced redox activity and the distinct adsorption behavior, which leads to a better catalytic performance, compared to $\text{Co}_H\text{Cu}/\text{Al}_2\text{O}_3$.

NH_3 emissions are expected to rise in the future from mobile vehicles and other industries, as there is increasing interest in using NH_3 as a sustainable fuel in particularly for shipping. Consequently, $\text{NH}_3\text{-SCO}$ to N_2 is a promising approach to help mitigate NH_3 emissions. To improve the performance of earth-abundant metal CoCu-based bimetallic catalysts, single Co sites were doped onto CuO NPs

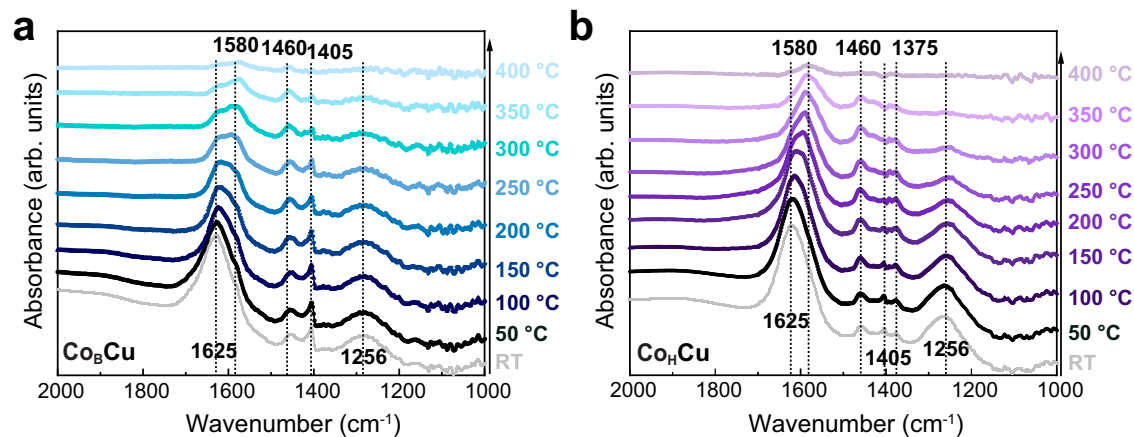


Fig. 6 | In-Situ DRIFTS spectra. In-Situ DRIFTS spectra of $\text{Co}_B\text{Cu}/\text{Al}_2\text{O}_3$ (a) and $\text{Co}_H\text{Cu}/\text{Al}_2\text{O}_3$ (b) as a function of temperature (the catalysts were exposed to a flow of 5000 ppm NH_3 and 5% O_2 for 20 min at different temperatures).

immobilized on an Al_2O_3 support, affording $\text{Co}_B\text{Cu}/\text{Al}_2\text{O}_3$ and $\text{Co}_H\text{Cu}/\text{Al}_2\text{O}_3$ catalysts with different electronic structures. Notably, the $\text{Co}_B\text{Cu}/\text{Al}_2\text{O}_3$ catalyst outperforms the $\text{Co}_H\text{Cu}/\text{Al}_2\text{O}_3$ catalysts with respect to both activity and selectivity, achieving full conversion of 5000 ppm NH_3 at 250 °C, with a selectivity to $\text{N}_2 > 80\%$, which is superior to the commercial 1% $\text{Pt}/\text{Al}_2\text{O}_3$ catalyst. The difference in the catalytic performance may be traced to differences in the electronic structure of the CuO NPs in $\text{Co}_B\text{Cu}/\text{Al}_2\text{O}_3$ and $\text{Co}_H\text{Cu}/\text{Al}_2\text{O}_3$ using advanced HERFD-XANES and VtC-XES techniques. The lower $1s \rightarrow 4p_z$ transition and higher $1s \rightarrow 4p$ transition ($K_{\beta_{2,5}}$ feature) of CuO in $\text{Co}_B\text{Cu}/\text{Al}_2\text{O}_3$ correlate with weaker Cu-O bonds, and these weaker bonds are related to longer Cu-O bonds lengths, as confirmed by STEM, EXAFS and wt-EXAFS. The weaker Cu-O bonds lead to enhanced redox properties of the CuO NPs, and enhanced NH_3 -SCO activity, further validated by *operando* XAS and in-situ NAP-NEXAFS studies. In contrast to the other catalysts, the oxidation state of the Cu center in $\text{Co}_B\text{Cu}/\text{Al}_2\text{O}_3$ is able to switch between Cu^{2+} and Cu^+ under all gas conditions and at all temperatures studied, which is vital for the catalyst to maintain good performance under real world conditions. Future studies will focus on upscaling and demonstrating the $\text{Co}_B\text{Cu}/\text{Al}_2\text{O}_3$ catalyst with real fuel gases.

Methods

Materials

$\text{Cu}(\text{NO}_3)_2 \cdot 3\text{H}_2\text{O}$, $\text{Co}(\text{NO}_3)_2 \cdot 6\text{H}_2\text{O}$, and NaBH_4 were purchased from Sigma Aldrich, and $\gamma\text{-Al}_2\text{O}_3$ was from Johnson Matthey. All chemicals are used as received.

Catalyst preparation

Synthesis of $\text{Co}_B\text{Cu}/\text{Al}_2\text{O}_3$. The $\text{Co}_B\text{Cu}/\text{Al}_2\text{O}_3$ catalyst was prepared via co-reduction of Co and Cu precursors using NaBH_4 as the reducing agent, followed by natural oxidation in the air. $\gamma\text{-Al}_2\text{O}_3$ (0.5 g, Johnson Matthey) was dispersed in H_2O (10 mL) under sonication for 30 min. Solution A containing $\text{Cu}(\text{NO}_3)_2 \cdot 3\text{H}_2\text{O}$ (100 mg) in H_2O (2 mL) and Solution B containing $\text{Co}(\text{NO}_3)_2 \cdot 6\text{H}_2\text{O}$ (2.5 mg) in H_2O (1 mL), were slowly added to the Al_2O_3 suspension, avoiding contact with air. After cooling in the ice bath, NaBH_4 (78 mg) in H_2O (2 mL) was added, and the resulting suspension was stirred for 30 min under N_2 . The resulting solid was collected by centrifugation and washed with H_2O (5×30 mL), and dried under vacuum, then followed by natural oxidation in the air to afford $\text{Co}_B\text{Cu}/\text{Al}_2\text{O}_3$.

Synthesis of $\text{Co}_H\text{Cu}/\text{Al}_2\text{O}_3$. The $\text{Co}_H\text{Cu}/\text{Al}_2\text{O}_3$ catalyst was prepared via co-reduction of Co and Cu precursors under H_2 , followed by natural oxidation in the air. $\gamma\text{-Al}_2\text{O}_3$ (0.5 g, Johnson Matthey) was dispersed in

H_2O (10 mL) under sonication for 30 min. Solution A containing $\text{Cu}(\text{NO}_3)_2 \cdot 3\text{H}_2\text{O}$ (100 mg) in H_2O (2 mL) and Solution B containing $\text{Co}(\text{NO}_3)_2 \cdot 6\text{H}_2\text{O}$ (2.5 mg) in H_2O (1 mL), were slowly added to the Al_2O_3 suspension. The resulting suspension was heated at 60 °C under stirring until all the solvent had evaporated. The remaining solid was heated to 300 °C for 1 h under 15% H_2/Ar at a heating rate of 5 °C/min in a tube furnace, then followed by natural oxidation in the air to afford $\text{Co}_H\text{Cu}/\text{Al}_2\text{O}_3$.

Synthesis of $\text{CuO}/\text{Al}_2\text{O}_3$. $\gamma\text{-Al}_2\text{O}_3$ (0.5 g, Johnson Matthey) was dispersed in H_2O (10 mL) with vigorous stirring at room temperature. To the resulting suspension, a solution containing $\text{Cu}(\text{NO}_3)_2 \cdot 3\text{H}_2\text{O}$ (100 mg) in H_2O (2 mL) was slowly added. The reaction mixture was then heated at 60 °C under stirring until all the solvent had evaporated. The remaining solid was heated to 300 °C for 1 h under 15% H_2/Ar at a heating rate of 5 °C/min in a tube furnace, then followed by natural oxidation in the air to afford $\text{CuO}/\text{Al}_2\text{O}_3$.

Synthesis of $\text{CoO}_x/\text{Al}_2\text{O}_3$. $\gamma\text{-Al}_2\text{O}_3$ (0.5 g, Johnson Matthey) was dispersed in H_2O (10 mL) under sonication for 30 min. Solution containing $\text{Co}(\text{NO}_3)_2 \cdot 6\text{H}_2\text{O}$ (130 mg) in H_2O (2 mL) was slowly added to the Al_2O_3 suspension. The resulting suspension was heated at 60 °C under stirring until all the solvent had evaporated. The remaining solid was heated to 300 °C for 1 h under 15% H_2/Ar at a heating rate of 5 °C/min in a tube furnace, then followed by natural oxidation in the air to afford $\text{CoO}_x/\text{Al}_2\text{O}_3$.

Synthesis of $\text{CoCu}/\text{Al}_2\text{O}_3$ (i.e., without reduction). $\gamma\text{-Al}_2\text{O}_3$ (0.5 g, Johnson Matthey) was dispersed in H_2O (10 mL) under sonication for 30 min. Solution A containing $\text{Cu}(\text{NO}_3)_2 \cdot 3\text{H}_2\text{O}$ (100 mg) in H_2O (2 mL) and Solution B containing $\text{Co}(\text{NO}_3)_2 \cdot 6\text{H}_2\text{O}$ (2.5 mg) in H_2O (1 mL), were slowly added to the Al_2O_3 suspension. The resulting suspension was heated at 60 °C under stirring until all the solvent had evaporated. The remaining solid is $\text{CoCu}/\text{Al}_2\text{O}_3$.

Ex situ characterization

X-ray diffraction (XRD) patterns were recorded using a StadiP diffractometer (STOE) equipped with a Mo source ($K\alpha = 0.7093165 \text{ \AA}$). The instrument operated at an applied voltage of 40 kV and a current of 30 mA. Diffraction data in the 2θ range of 2–40° were systematically collected, with a resolution of 0.015° per step.

X-ray photoelectron spectroscopy (XPS) was conducted using a Thermo Fisher Scientific NEXSA spectrometer. The C 1s peak at 284.8 eV served as the standard reference for calibrating the photoelectron energy shift. CasaXPS software was used for data analysis.

Energy dispersive X-ray (EDX) spectroscopy and aberration-corrected bright field (BF) imaging were performed on a JEOL ARM200CF (E01) operating at 200 kV and equipped with JEOL dual silicon drift detectors at the electron Physical Sciences Imaging Centre (ePSIC) at the Diamond Light Source (DLS) (UK). The instrument operated with a convergence semi-angle of 23.0 mrad with BF collection semi-angles of 0–21.9. Single-pass EDX spectra were collected with drift correction. Data were acquired and processed using the Gatan Microscopy Suite (a.k.a. Digital Micrograph)⁶⁰. Samples were prepared via a standard preparation route: a small amount (<20 mg) of catalyst powder was dispersed in approximately 5 ml of ethanol, after sonication and drop casting approximately 1 ml of supernatant onto holey carbon-coated, gold TEM support grids. Gold was used instead of the more typical copper grid to avoid overlapping fluorescent signals with the sample during EDX mapping. The average particle size was calculated based on more than 100 particles for each sample.

HERFD-XANES measurements were conducted at the I20-Scanning beamline at the DLS (UK). The X-ray beam was introduced through Rh-coated optic hutch mirrors, and a Si(111) scanning four-bounce monochromator was employed to select the incident energy. HERFD-XANES spectra were obtained by scanning the incident energy across the range 8800.00 to 9400.00 eV with a step size of 0.15 eV. Samples were homogenized with boron nitride and compressed into pellets with a diameter of 8 mm. XANES analysis was carried out using the Demeter software package.

Extended X-ray absorption fine structure (EXAFS) of the Co K-edge (7709 eV) and Cu K-edge (8979 eV) were carried out at the DLS (UK) and Spring8 (Japan). Samples were directly pressed into pellets for fluorescence measurements of the Co K-edge and transmission measurements of the Cu K-edge. Co foil or Cu foil standards were used for energy shift calibration. XAFS data were merged from 3 spectra to improve signal quality and were processed using the Demeter software package (including Athena and Artemis). Athena software was used to analyze the XANES data. Artemis software was used to fit the k^2 -weighted EXAFS data in real space with $3.0 \text{ \AA}^{-1} < k < 12.0 \text{ \AA}^{-1}$ and $1.0 \text{ \AA} < R < 3.3 \text{ \AA}$. The calculated amplitude reduction factor, S_0^2 , from the EXAFS analysis of Cu and Co foil was 0.878 and 0.879, respectively, and were used as fixed parameters for EXAFS fitting. The coordination number and bond length were calculated based on the reported structures from the Crystal open database: Cu (No. 9013014), CuO (No. 1011148), Co (No. 9008492), and Co_3O_4 (No. 9005898).

Operando Co K-edge and Cu K-edge XAFS

Operando XAFS experiments were performed at the Spring8 beamline (Japan). 100 mg of pelletized catalysts were measured at 8780–10200 eV for Cu K edge in transmission mode and 7505–8670 eV for Co K-edge in fluorescence mode at different temperatures and under various gas atmospheres. The pelletized catalyst was exposed to 5000 ppm NH_3 and 5% O_2 in He (total gas flow rate 100 mL/min) at different temperature from 30 °C to 450 °C. For experiments carried out under various gas atmospheres at 200 °C, the sequence of different gas atmospheres follows $\text{NH}_3 + \text{O}_2$ (5000 ppm NH_3 and 5% O_2 in He), NH_3 (5000 ppm NH_3 in He), $\text{NH}_3 + \text{O}_2$ (5000 ppm NH_3 and 5% O_2 in He), and O_2 (5% O_2 in He). All spectra were recorded under steady-state conditions. Spectra processing was performed with Athena software.

In-situ DRIFTS

DRIFTS were performed on a PerkinElmer Frontier FT-IR Spectrometer. The sample was heated in He at 350 °C for 30 min to remove surface contamination. After cooling to room temperature, the sample was exposed to 5000 ppm NH_3 and 5% O_2 in He (total gas flow rate 100 mL/min), for 30 min, during which spectra were recorded. Then, the sample was heated from 30 °C to 450 °C with a temperature ramp of 10 °C/min. The spectra were recorded from 4400 to 500 cm^{-1} with a

resolution of 2 cm^{-1} . Background spectra were recorded in He and subtracted from the sample spectrum for each measurement.

In situ near-edge X-ray absorption fine structure (NEXAFS) spectroscopy

In situ NEXAFS experiments were performed on the B07 beamline at the DLS (UK)⁶¹. The X-ray radiation was sourced from a bending magnet and a plane grating monochromator (PGM) with an energy range from 110 to 2800 eV (soft X-ray range) and flux of $>10^{10}$ photons/s with 0.3 A ring current. The reaction products were monitored online using an electron impact mass spectrometer (Hiden HMT100) connected directly to the prelens chamber. The pressure in the specimen chamber was precisely controlled (HV or 0.1–1 mbar) by simultaneous operation of several mass flow controllers for reactive gases and a PID-controlled throttle valve acting as back pressure controller. Temperature control was provided by two K-type thermocouples. NEXAFS spectra at Cu L-edge (925–940 eV) were measured in Auger electron yield (AEY) mode using a SPECS phoibos 150 hemispherical analyser set.

Catalytic performance measurements

The performance of the catalysts in the NH_3 -SCO reaction was evaluated in a fixed-bed flow reactor at a gas flow rate of 100 mL/min, which consists of 5000 ppm NH_3 , 5% O_2 , and He balance. Typically, 50 mg of catalyst was placed in the reaction tube, and the quantification of products was performed with an online quadrupole mass spectrometer quantitative gas analyzer (Hiden Analytical, UK). The reactions were investigated at temperatures ranging from 100 to 450 °C and kept stable for at least 30 min after attaining a steady state at each reaction temperature to detect the MS signals of NH_3 and O_2 and the products, i.e., N_2 , N_2O , and NO. Stability test: 50 mg $\text{Co}_B\text{Cu}/\text{Al}_2\text{O}_3$ and 100 mg SiC were mixed by grinding and then tested for 4 cycles.

Data availability

All data generated in this study are provided in the Supplementary Information. Data are available from the corresponding authors upon request.

References

1. Van Damme, M. et al. Industrial and agricultural ammonia point sources exposed. *Nature* **564**, 99–103 (2018).
2. Chen, Z. L. et al. Significant contributions of combustion-related sources to ammonia emissions. *Nat. Commun.* **13**, 1–10 (2022).
3. Plautz, J. Piercing the haze: Ammonia, a poorly understood smog ingredient, could be key to limiting deadly particulate pollution. *Science* (1979) **361**, 1060–1063 (2018).
4. Ma, R. et al. Mitigation potential of global ammonia emissions and related health impacts in the trade network. *Nat. Commun.* **12**, 1–13 (2021).
5. Dann, E. K. et al. Structural selectivity of supported Pd nanoparticles for catalytic NH_3 oxidation resolved using combined operando spectroscopy. *Nat. Catal.* **2**, 157–163 (2019).
6. Brandenberger, S., Kröcher, O., Tissler, A. & Althoff, R. The state of the art in selective catalytic reduction of NOx by ammonia using metal-exchanged zeolite catalysts. *Catal. Rev.* **50**, 492–531 (2008).
7. Han, L. et al. Selective catalytic reduction of NOx with NH_3 by using novel catalysts: state of the art and future prospects. *Chem. Rev.* **119**, 10916–10976 (2019).
8. Wang, J., Zhao, H., Haller, G. & Li, Y. Recent advances in the selective catalytic reduction of NOx with NH_3 on Cu-Chabazite catalysts. *Appl Catal. B.* **202**, 346–354 (2017).
9. Gao, F. et al. Advances in selective catalytic oxidation of ammonia (NH_3 -SCO) to dinitrogen in excess oxygen: A review on typical catalysts, catalytic performances and reaction mechanisms. *J. Environ. Chem. Eng.* **9**, 104575 (2021).

- Lan, T. et al. Selective catalytic oxidation of NH₃ over noble metal-based catalysts: state of the art and future prospects. *Catal. Sci. Technol.* **10**, 5792–5810 (2020).
- Jabłońska, M. Progress on selective catalytic ammonia oxidation (NH₃-SCO) over Cu-containing zeolite-based catalysts. *Chem-CatChem* **12**, 4490–4500 (2020).
- Cui, X. et al. Selective catalytic oxidation of ammonia to nitrogen over mesoporous CuO/RuO₂ synthesized by co-nanocasting-replication method. *J. Catal.* **270**, 310–317 (2010).
- Curtin, T. et al. The catalytic oxidation of ammonia: Influence of water and sulfur on selectivity to nitrogen over promoted copper oxide/alumina catalysts. *Catal. Today* **55**, 189–195 (2000).
- Chmielarz, L. et al. Selective catalytic oxidation of ammonia to nitrogen over Mg-Al, Cu-Mg-Al and Fe-Mg-Al mixed metal oxides doped with noble metals. *Appl. Catal. B* **130–131**, 152–162 (2013).
- Burch, R. & Southward, B. W. L. Low-temperature, lean catalytic combustion of N-bearing gasified biomass using a novel NH₃ trapping catalyst. *Chem. Commun.* **2**, 1115–1116 (2000).
- Guan, X. et al. Designing Reactive Bridging O₂-at the Atomic Cu-O-Fe Site for Selective NH₃ Oxidation. *ACS Catal.* **12**, 15207–15217 (2022).
- Paolucci, C. et al. Dynamic multinuclear sites formed by mobilized copper ions in NO_x selective catalytic reduction. *Science (1979)* **357**, 898–903 (2017).
- Marberger, A. et al. Time-resolved copper speciation during selective catalytic reduction of NO on Cu-SSZ-13. *Nat. Catal.* **1**, 221–227 (2018).
- Lomachenko, K. A. et al. The Cu-CHA deNO_x catalyst in action: temperature-dependent NH₃-assisted selective catalytic reduction monitored by Operando XAS and XES. *J. Am. Chem. Soc.* **138**, 12025–12028 (2016).
- Krishna, S. H. et al. Influence of framework Al density in chabazite zeolites on copper ion mobility and reactivity during NO_x selective catalytic reduction with NH₃. *Nat. Catal.* **6**, 276–285 (2023).
- Gao, F., Mei, D., Wang, Y., Szanyi, J. & Peden, C. H. F. Selective catalytic reduction over Cu/SSZ-13: linking homo- and heterogeneous catalysis. *J. Am. Chem. Soc.* **139**, 4935–4942 (2017).
- Fung, W.-K., Ledwaba, L., Modiba, N., Claeys, M. & van Steen, E. Choosing a suitable support for Co₃O₄ as an NH₃ oxidation catalyst. *Catal. Sci. Technol.* **3**, 1905 (2013).
- Fung, W.-K., Claeys, M. & van Steen, E. Effective utilization of the catalytically active phase: NH₃ oxidation over unsupported and supported Co₃O₄. *Catal. Lett.* **142**, 445–451 (2012).
- Sadykov, V. A. et al. Oxide catalysts for ammonia oxidation in nitric acid production: properties and perspectives. *Appl. Catal. A Gen.* **204**, 59–87 (2000).
- Schmidt-Szałowski, K., Krawczyk, K. & Petryk, J. The properties of cobalt oxide catalyst for ammonia oxidation. *Appl. Catal. A Gen.* **175**, 147–157 (1998).
- Petryk, J. & Kolakowska, E. Cobalt oxide catalysts for ammonia oxidation activated with cerium and lanthanum. *Appl. Catal. B* **24**, 121–128 (2000).
- Liu, Y. et al. Unraveling the Lattice O-assisted internal selective catalytic reduction mechanism on high N₂ selectivity of CuOx/PtCu catalysts in NH₃-SCO. *ACS Catal.* <https://doi.org/10.1021/ACSCATAL.3C00314>. (2023).
- Sun, M. et al. Promotion of catalytic performance by adding Cu into Pt/ZSM-5 catalyst for selective catalytic oxidation of ammonia. *J. Taiwan Inst. Chem. Eng.* **78**, 401–408 (2017).
- Dhillon, P. S., Harold, M. P., Wang, D., Kumar, A. & Joshi, S. Y. Enhanced transport in washcoated monoliths: Application to selective lean NO_x reduction and ammonia oxidation. *Chem. Eng. J.* **377**, 119734 (2019).
- Qu, Z., Wang, Z., Quan, X., Wang, H. & Shu, Y. Selective catalytic oxidation of ammonia to N₂ over wire-mesh honeycomb catalyst in simulated synthetic ammonia stream. *Chem. Eng. J.* **233**, 233–241 (2013).
- Zhou, M. et al. High-Performance Ag-Cu Nanoalloy Catalyst for the Selective Catalytic Oxidation of Ammonia. *ACS Appl. Mater. Interfaces* **11**, 46875–46885 (2019).
- Lin, S. D., Gluhoi, A. C. & Nieuwenhuys, B. E. Ammonia oxidation over Au/MOx/γ-Al₂O₃—activity, selectivity and FTIR measurements. *Catal. Today* **90**, 3–14 (2004).
- Cui, X. et al. Fabrication of hierarchically porous RuO₂-CuO/Al-ZrO₂ composite as highly efficient catalyst for ammonia-selective catalytic oxidation. *ACS Catal.* **4**, 2195–2206 (2014).
- Tang, X. et al. An Efficient Two-Step Method for NH₃ Removal at Low Temperature Using CoOx-CuOx/TiO₂ as SCO Catalyst Followed by NiMn₂O₄ as SCR Catalyst. *Energy Fuels* **31**, 8580–8593 (2017).
- Chen, Z. & Zhang, P. Electronic structure of single-atom alloys and its impact on the catalytic activities. *ACS Omega* **7**, 1585–1594 (2022).
- Liu, K. et al. Electronic effects determine the selectivity of planar Au-Cu bimetallic thin films for electrochemical CO₂ reduction. *ACS Appl. Mater. Interfaces* **11**, 16546–16555 (2019).
- Xiong, M. et al. In situ tuning of electronic structure of catalysts using controllable hydrogen spillover for enhanced selectivity. *Nat. Commun.* **11**, 1–10 (2020).
- Slavinskaya, E. M. et al. Studies of the mechanism of ammonia oxidation into nitrous oxide over MnBiO/α-Al₂O₃ catalyst. *J. Catal.* **222**, 129–142 (2004).
- Il'chenko, N. I. & Golodets, G. I. Catalytic oxidation of ammonia: I. Reaction kinetics and mechanism. *J. Catal.* **39**, 57–72 (1975).
- Zhang, T., Walsh, A. G., Yu, J. & Zhang, P. Single-atom alloy catalysts: structural analysis, electronic properties and catalytic activities. *Chem. Soc. Rev.* **50**, 569 (2021).
- Ding, M. et al. Effect of reducing agents on microstructure and catalytic performance of precipitated iron-manganese catalyst for Fischer-Tropsch synthesis. *Fuel Process. Technol.* **92**, 2353–2359 (2011).
- Wu, Y. et al. Effect of reducing agent on the structure and activity of manganese oxide octahedral molecular sieve (OMS-2) in catalytic combustion of o-xylene. *Catal. Today* **281**, 500–506 (2017).
- Yu, K., Lou, L., Liu, S. & Zhou, W. Asymmetric oxygen vacancies: the intrinsic redox active sites in metal oxide catalysts. *Adv. Sci.* **7**, 1901970 (2020).
- Kang, L. et al. Adsorption and activation of molecular oxygen over atomic copper(I/II) site on ceria. *Nat. Commun.* **11**, 4008 (2020).
- Vegeius, J. R., Kvashnina, K. O., Klintenber, M., Soroka, I. L. & Butorin, S. M. Cu Kβ 2,5 X-ray emission spectroscopy as a tool for characterization of monovalent copper compounds. *J. Anal. Spectrom.* **27**, 1882–1888 (2012).
- Chen, L. et al. Tuning the selectivity of NH₃ oxidation via cooperative electronic interactions between platinum and copper sites. *Nat. Commun.* **16**, 1–9 (2025).
- Jabłońska, M. & Palkovits, R. Copper based catalysts for the selective ammonia oxidation into nitrogen and water vapour—Recent trends and open challenges. *Appl. Catal. B* **181**, 332–351 (2016).
- Yao, P. et al. Engineering a PtCu alloy to improve N₂ selectivity of NH₃-SCO over the Pt/SSZ-13 catalyst. *ACS Appl. Mater. Interfaces* **16**, 14694–14703 (2024).
- An, Q. et al. Designing a bifunctional Pt/Cu-SSZ-13 catalyst for ammonia-selective catalytic oxidation with superior selectivity. *ACS Catal.* **13**, 6851–6861 (2023).
- Decarolis, D. et al. Spatial profiling of a Pd/Al₂O₃ catalyst during selective ammonia oxidation. *ACS Catal.* **11**, 2141–2149 (2021).
- Curtin, T. & Lenihan, S. Copper exchanged beta zeolites for the catalytic oxidation of ammonia. *Chem. Commun.* **3**, 1280–1281 (2003).
- Baker, M. L. et al. K- and L-edge X-ray absorption spectroscopy (XAS) and resonant inelastic X-ray scattering (RIXS) determination

- of differential orbital covalency (DOC) of transition metal sites. *Coord. Chem. Rev.* **345**, 182–208 (2017).
53. Geoghegan, B. L. et al. Combining valence-to-core X-ray emission and Cu K-edge X-ray absorption Spectroscopies to experimentally assess oxidation state in organometallic Cu(I)/(II)/(III) complexes. *J. Am. Chem. Soc.* **144**, 2520–2534 (2022).
54. Tomson, N. C. et al. Re-evaluating the Cu K pre-edge XAS transition in complexes with covalent metal-ligand interactions. *Chem. Sci.* **6**, 2474–2487 (2015).
55. Wu, Y. et al. Interplay between copper redox and transfer and support acidity and topology in low temperature NH₃-SCR. *Nat. Commun.* **14**, 2633 (2023).
56. Chen, L. et al. Thermally stable high-loading single Cu sites on ZSM-5 for selective catalytic oxidation of NH₃. *Proc. Natl. Acad. Sci. USA* **121**, e2404830121 (2024).
57. Burch, R. & Southward, B. W. L. A novel application of trapping catalysts for the selective low-temperature oxidation of NH₃ to N₂ in simulated biogas. *J. Catal.* **195**, 217–226 (2000).
58. Zhang, Q. et al. In situ DRIFTS studies on CuO-Fe₂O₃ catalysts for low temperature selective catalytic oxidation of ammonia to nitrogen. *Appl. Surf. Sci.* **419**, 733–743 (2017).
59. Yang, J. et al. Time-resolved in situ DRIFTS study on NH₃-SCR of NO on a CeO₂/TiO₂ catalyst. *Catal. Sci. Technol.* **12**, 1245–1256 (2022).
60. DigitalMicrograph Software. <https://www.gatan.com/products/tem-analysis/gatan-microscopy-suite-software>.
61. Held, G. et al. Ambient-pressure endstation of the Versatile Soft X-ray (VerSoX) beamline at Diamond Light Source. *J. Synchrotron. Radiat.* **27**, 1153–1166 (2020).

Acknowledgements

We thank the EPSRC for the UKRI Postdoctoral Fellowship (MSCA) to Lu Chen (EP/X022986/1). We thank the EPSRC (EP/S018204/2, EP/Z001730/1 and EP/Y036220/1) for financial support. We thank the Isaac Newton Trust Grant (24.24(h)), University of Cambridge. We thank the beamline scientists at the SPring-8 (BL14B2) and Diamond Light Source for the provision of beamtimes (I20-Scanning: SP30576-1, B07: SI31867). We thank the scientists in the Electron Physical Science Imaging Centre (EPSIC: MG32996). XAS measurements were performed at BL14B2 of SPring-8 with the approval of the Japan Synchrotron Radiation Research Institute (JASRI) (Proposal No. 2022B1758). We thank Soleil synchrotron (Galaxies beamline 20221122), European Synchrotron Radiation Facility (ESRF) CH6856 and MAX IV (Balder beamline 20230511). We thank the UK Catalysis Hub for the provision of DRIFTS. We thank Dr. Shaoliang Guan (Maxwell Centre, University of Cambridge) for the XPS measurements.

Author contributions

L.C. and X.G. conceived of the presented idea. L.C. and F.R.W. secured the funding. L.C. carried out catalyst synthesis and catalytic evaluations

and X.G. verified the analytical methods. L.C., X.G. and F.R.W. carried out the operando XAS study and L.C. and X.G. analyzed the data. L.C. conducted the XRD measurements and the XPS measurements. HERFD-XANES and VtC-XES studies were supported by S.H. L.C. and X.G. carried out the NAP-NEXAFS studies with support from M.V.S., B.K. and G.H. X.G., C.A. and D.H. conducted the TEM measurements. L.C., X.G. performed DRIFTS experiments with the support of J.C. L.C. and P.J.D. wrote the paper and all authors contributed to the final manuscript.

Competing interests

The authors declare no competing interests.

Additional information

Supplementary information The online version contains supplementary material available at <https://doi.org/10.1038/s41467-025-64415-w>.

Correspondence and requests for materials should be addressed to Lu Chen, Paul J. Dyson or Feng Ryan Wang.

Peer review information *Nature Communications* thanks Haidi Xu and the other anonymous reviewer(s) for their contribution to the peer review of this work. A peer review file is available.

Reprints and permissions information is available at <http://www.nature.com/reprints>

Publisher's note Springer Nature remains neutral with regard to jurisdictional claims in published maps and institutional affiliations.

Open Access This article is licensed under a Creative Commons Attribution 4.0 International License, which permits use, sharing, adaptation, distribution and reproduction in any medium or format, as long as you give appropriate credit to the original author(s) and the source, provide a link to the Creative Commons licence, and indicate if changes were made. The images or other third party material in this article are included in the article's Creative Commons licence, unless indicated otherwise in a credit line to the material. If material is not included in the article's Creative Commons licence and your intended use is not permitted by statutory regulation or exceeds the permitted use, you will need to obtain permission directly from the copyright holder. To view a copy of this licence, visit <http://creativecommons.org/licenses/by/4.0/>.

© The Author(s) 2025